Acta Astronautica 192 (2022) 1–14

Contents lists available at ScienceDirect

Acta Astronautica

journal homepage: www.elsevier.com/locate/actaastro

Thermochemical non-equilibrium effects on hypersonic shock wave/turbulent boundary-layer interaction

Hao Jiang [a], Jun Liu [a,*], Shichao Luo [a], Wei Huang [a], Junyuan Wang [a], Meikuan Liu [b]

[a] Science and Technology on Scramjet Laboratory, National University of Defense Technology, Changsha, 410073, China
[b] State Key Laboratory of High Temperature Gas Dynamics, Institute of Mechanics, Chinese Academy of Sciences, Beijing, 100190, China

ARTICLE INFO

Keywords:
Hypersonic flow
Shock wave/turbulent boundary-layer interactions
Thermochemical non-equilibrium
Turbulence model

ABSTRACT

The research on shock wave/turbulent boundary-layer interactions is mainly limited to calorically perfect gases; little has been reported on the thermochemical non-equilibrium (real gas) effect. This effect is prominent at conditions of high Mach and Reynolds numbers. In this work, a household parallel solver for hypersonic thermochemical non-equilibrium flows with a Reynolds-averaged Navier–Stokes turbulence model is developed in which the coupling of turbulence with vibration and chemistry occurs under a gradient-law assumption. The thermal non-equilibrium is based on Park's two-temperature model, and the chemical non-equilibrium is based on Gupta's 11-species model. The method proposed in this paper is first validated using experimental data, including cases of a laminar cylinder flow at a high-enthalpy condition, a supersonic flat-plate turbulent boundary layer flow, a hypersonic transition flow, and a hypersonic compression corner flow at a low-enthalpy condition. This approach is then applied to assess the hypersonic flow characteristics past the 34° compression corner at a flight height of 30 km. Results show that the joint effects of turbulence and thermochemical non-equilibrium have a significant impact on the flow field organization, wall data, and separation length of the shock wave/boundary-layer interaction. Furthermore, the mechanism of the neck region accompanied by maximum heat flux, wall pressure and skin friction in both laminar and turbulent cases is well-interpreted. This study can be used as a reference tool for the aerodynamic design of future hypersonic vehicles accounting for multi-physics effects.

1. Introduction

The compression corner is a typical configuration for control surfaces in external flow fields of hypersonic vehicles wherein a shock wave/boundary-layer interaction occurs [1,2]. The strong adverse pressure gradient brought about by the compression wave system causes the boundary layer to separate and leads to an abrupt rise in wall-heat transfer, degraded performance of control surfaces, and sometimes disastrous accidents. Moreover, during hypersonic flights in the relatively lower layers of near space (20–40 km), this phenomenon becomes more serious because the laminar boundary-layer transits to turbulent boundary-layer as the Reynolds number exceeds the transition threshold [3,4]. This so-called shock wave/turbulent boundary-layer interaction (STBLI) is accompanied with amplifications of the heat flux and drag [5], depicted in Fig. 1.

As the next generation of hypersonic vehicles become capable of reaching higher Mach (*Ma*) numbers in the relatively lower layers of near space, massive amounts of kinetic energy from the freestream are converted into internal energy in the STBLI zones, which brings about complex physical and chemical phenomena, such as vibrational excitation, gas dissociation, and ionization. In such conditions, the gas may not always be treated as a perfect gas (PG), but as a real gas (RG). When the characteristic time of the flow field is the same order of magnitude as the molecular vibration relaxation time and the chemical reaction time, the flow is classified as a thermochemical non-equilibrium (TCNE) flow [8]. This TCNE not only significantly alters the inviscid flow, but it also affects the turbulent flow [9] and the complex STBLI flow. Additionally, the extreme conditions of hypersonic flight are beyond the performance envelopes of the present hypersonic facilities needed to cover high enthalpy and high Mach and Reynolds numbers. The thermal protection system margin [10], which is based on ground-test extrapolation-to--flight, is not reliable. Graham [11] commented that little effort had been directed toward understanding turbulent motion at the extreme conditions of hypersonic flight. Therefore, performing reliable numerical simulations is necessary to compensate for the lack of experimental data.

* Corresponding author.
E-mail address: liujun@nudt.edu.cn (J. Liu).

https://doi.org/10.1016/j.actaastro.2021.12.010
Received 14 September 2021; Received in revised form 21 November 2021; Accepted 5 December 2021
Available online 7 December 2021
0094-5765/© 2021 IAA. Published by Elsevier Ltd. All rights reserved.

Nomenclature

Ma	Mach number
H	flight height
x, y, z	Cartesian coordinates
Re	Reynolds number
$\mathrm{Re}_{\mathrm{tr}}$	transition Reynolds number
Re_x	Reynolds number based on x
L	reference length
ρ	total density of the gas mixture
ρ_k	density of species k
Y_k	mass fraction of species k
ns	total number of species
mol	total number of molecular species
u_j	vector components of gas velocity
$J_{k,j}$	vector components of the diffusion flux of the species k
$\dot{\omega}_k$	mass rate of production of species k
p	pressure
τ_{ij}	total stresses tensor deviator
δ_{ij}	the Kronecker symbol
E	total energy of the gas mixture
e_k	internal energy of species k
$e_{v,k}$	vibrational energy of species k
e_v	total vibrational energy of the gas mixture
S_v	vibrational energy source term
h	total enthalpy of the gas mixture
h_k	total enthalpy of species k
q_j	vector components of the total heat flux
q_j^L	vector components of the laminar heat flux
q_j^T	vector components of the turbulent heat flux
$q_{v,j}$	vector components of the total vibrational heat flux
$q_{v,j}^L$	vector components of the laminar and vibrational heat flux
$q_{v,j}^T$	vector components of the turbulent and vibrational heat flux
T	transitional-rotational temperature
T_v	vibrational temperature
T_w	wall temperature
μ_L	laminar viscosity
μ_T	turbulent viscosity
k_{tr}	the thermal conductivity for transitional energy
k_v	the thermal conductivity for vibrational energy
$D_{L,k}$	laminar diffusion coefficient of species k
Cp_{tr}	transitional-rotational part of the specific heat at constant pressure
Cp_v	vibrational part of the specific heat at constant pressure
Pr_T	turbulent Prandtl number
Sc_T	turbulent Schmidt number
K	turbulent kinetic energy of fluctuations
ω	the rate of dissipation of energy
δ	boundary layer thickness
α	recompression shock angle
U_∞	inflow velocity
ρ_∞	inflow density
p_w	wall pressure
p_∞	inflow pressure
q_w	wall heat flux
q_∞	inflow heat flux
C_f	skin friction coefficient
STBLI	shock wave/turbulent boundary layer interaction
TCNE	thermochemical non-equilibrium
RG	real gas
PG	perfect gas
RANS	Reynolds-averaged Navier–Stokes
DNS	direct numerical simulation

Subscripts

∞	freestream
k	species

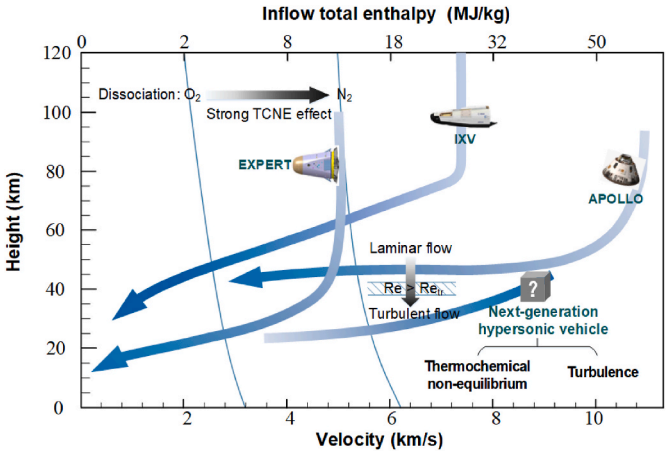

Fig. 1. Typical trajectories of various hypersonic vehicles with thermochemical non-equilibrium and turbulence effects [6,7].

With respect to the chemical nonequilibrium effect on the turbulence, a few direct numerical simulation (DNS) studies have been carried out, in which objects of these studies are simple such as turbulent boundary layers on the flat-plate and turbulent channel flows [9,12–14]. Chen and Li [12] studied the turbulent statistical characteristics of high-enthalpy turbulent channel flows at $Ma = 6$ and 10. Duan and Martin [13,14] performed DNSs of the high-enthalpy turbulent boundary layer in a small subdomain of a wedge at $Ma = 21$ and an altitude of 30 km. Passiatore [9] investigated finite-rate chemistry effects in high-enthalpy boundary layers of $Ma = 10$ flows by using a chemically reacting model of five species. They concluded that the chemical reactions affected the first-order statistics of thermodynamic quantities, but did not have sizable influence on turbulent kinetic energy budgets or on the turbulence structure. The gradient transport model approximately holds with turbulent Prandtl and Schmidt numbers of near unit value, and is thus adopted in our model.

With respect to the TCNE effect on STBLI, extensive research has been carried out under the calorically perfect gas assumption [15–19] or in terms of shock wave/laminar boundary layer interaction that consider the TCNE effect but without turbulence [20–23]. For example, Zhu et al. [18,19] carried out high-accuracy simulations of shock wave/turbulent boundary layer interaction on a flat plate considering different added periodic disturbances and wall temperatures. Clemente et al. [22] numerically investigated the shock wave/boundary layer interaction phenomenon occurring around the full-scale EXPERT 20-degree flap, where the TCNE effects are considered using a chemically reacting model of five species in the absence of ionization and turbulence. Zuo and Hu [23] investigated hypersonic non-equilibrium air flows over a laminar double-cone configuration. These studies [20–23] have concluded that the TCNE effect may yield a reduction in separation length, depending on the freestream dissociation to the shock wave/-laminar boundary layer interaction.

Moreover, various control methods [24–27] have shown promising effects in shock wave/boundary layer interaction control, such as mitigation of shock wave, reduction in separation length, and reduction of average value of the wall heat flux. Wang et al. [24] studied experimentally and numerically the control ability of a quasi-direct current discharge method on the shock wave/boundary layer interaction induced by a compression corner. Jiang et al. [25] proposed a novel magnetohydrodynamic interaction parameter for predicting the STBLI control ability based on Lorentz acceleration actuator. Besides, previous studies of air-breathing hypersonic vehicles [28,29] were using the perfect gas model in which the local unstart of hypersonic inlet is closely related to shock wave/boundary layer interaction.

From the preceding literature survey, the abovementioned works merely focus on how the TCNE effect influences the STBLI, which is not fully understood and remains a state-of-the-art research problem. Nor do the examinations of the active control or the aerodynamics design consider multi-physics effects. Only recently was the oblique STBLI by means of DNS in only chemical nonequilibrium conducted by Volpiani [30]. However, as with other DNS studies of simple configurations, the thermal nonequilibrium was not considered, and computations were at moderate Reynolds number and $Ma = 5.6$ with weak shock strength.

Other related research mainly focuses on the utilization of Reynolds-averaged Navier–Stokes (RANS) method to study the TCNE effect on STBLI. This is mainly due to the incredibly huge computation demands of DNSs in simulations with multi-physics, while the RANS method still remains a feasible tool in engineering design. Grasso et al. [31] studied the turbulence and wall-temperature effects of STBLI in the presence of TCNE using a k-ε two-equation turbulence model. The configuration was a 2-dimensional geometry corresponding to the symmetry plane of a reusable launch vehicle. Inflow conditions were $H = 51.9$ km, $Ma = 9.99$, and $\mathrm{Re/m} = 1.578 \times 10^5$, where the transition was triggered at about one-third of the vehicle length (42.5 m). However, the differences of shock wave/boundary layer interaction structures around the flap under laminar and turbulent conditions were not fully discussed, and the entropy layer effect from the blunt nose was not excluded. Wang et al. [32] utilized a thermochemical non-equilibrium model and a perfect gas model to investigate the aerothermodynamics of Mars entry vehicle at $Ma = 26.1$. The results showed that the flow structure and heating rates at the vehicle's body are heavily influenced by the two gas models. However, the inflow gas species were the Martian species, and STBLI was not obvious in the flow structure. Owing to the small level of thermal nonequilibrium in the Martian atmosphere, one temperature model was used for the computation. Jiang and Yan [33] conducted computations of STBLI flows using a shear transport turbulence (SST) model under a thermally perfect gas assumption. It was mentioned that extending the thermally perfect gas model to the TCNE model would be more appropriate for high-enthalpy cases. Dai et al. [34] numerically investigated the influence of the real gas effect on the Mach 12 flow of the inward-turning inlet using three gas models of thermally perfect, chemical non-equilibrium, and TCNE, it was notable that the dissociation degree of oxygen reaches 54.8% at the symmetry plane using TCNE model. Moreover, a 5-species air model was used in their study while the coupling of the turbulence model with the Navier-Stokes equations should be better described in detail.

In this paper, the immediate objective is to study the TCNE effect on the STBLI that occurs on typical configurations of hypersonic vehicles by means of our novel numerical framework in which the mechanism needs to be further understood from a physical perspective. A baseline STBLI case considering TCNE is first conducted using a 34° compression corner at a flight height of 30 km at Ma 20. A companion RANS case is run at the same free-stream conditions and wall temperature by assuming a calorically perfect gas composition and transport properties. The second companion case is run at the same conditions as the baseline but under the laminar assumption. These tests allow isolation of the contributions of TCNE and turbulence effects, respectively, via the direct comparison of the three cases.

The paper is structured as follows. Model descriptions are provided in Section 2. Validations and assessments of the solver are discussed in Section 3. A grid sensitivity study and the error estimation are investigated in Section 4. An analysis of shock wave/boundary layer interactions considering the effects of thermochemical non-equilibrium and flight Mach number is investigated in Section 5. Finally, the conclusions are drawn in Section 6.

2. Mathematical model

2.1. Governing equations

For compressible flows with a calorically perfect gas assumption, the RANS method is often utilized to model the effect of turbulent fluctuations on average flow by adding turbulence stress items to the averaged momentum equation [35]. Meanwhile, the RANS method coupled with the chemical non-equilibrium effect has been well established and applied in detonation research [36,37]. Further, the RANS method coupled with the TCNE effect has been receiving considerable attention, owing to the aerodynamics problems encountered in engineering [7].

To further extend the turbulent viscosity model from calorically perfect gas flows to hypersonic TCNE flows, theoretical derivations, reasonable modeling, and model calibration using reliable high-enthalpy test data are needed. The current study focuses on the first two aspects because of a lack of available high-enthalpy test data. In this study, a novel parallel non-equilibrium solver with a turbulence model is developed and deployed to analyze STBLIs. This method, but without a turbulence model has been tested and verified in our previous studies [10,38,39]. The detailed models are presented below.

By introducing both Favre and conventional time averages [31] into the governing equations, the Reynolds-averaged formulation of the conservation laws in Cartesian coordinates can be obtained as follows:

$$\frac{\partial \rho_k}{\partial t} + \frac{\partial}{\partial x_j}\left(\rho_k u_j\right) - \frac{\partial J_{kj}}{\partial x_j} = \dot{\omega}_k \tag{1}$$

$$\frac{\partial}{\partial t}\left(\rho u_i\right) + \frac{\partial}{\partial x_j}\left(\rho u_i u_j + p\delta_{ij}\right) - \frac{\partial \tau_{ij}}{\partial x_j} = 0 \tag{2}$$

$$\frac{\partial \rho E}{\partial t} + \frac{\partial}{\partial x_j}\left[u_j(\rho E + p)\right] - \frac{\partial}{\partial x_j}\left(q_j + u_i \tau_{ij}\right) = 0 \tag{3}$$

$$\frac{\partial \rho e_v}{\partial t} + \frac{\partial}{\partial x_j}\left(\rho e_v u_j\right) - \frac{\partial}{\partial x_j}\left(q_{v,j}\right) = S_v \tag{4}$$

Here, the species index k varies from 1 to ns, ρ_k is the density of a species k, ρ is the total density of the gas mixture, u_j are the vector components of gas velocity, J_{kj} are the vector components of the diffusion flux of species k, $\dot{\omega}_k$ is the mass rate of production of species k, p is the mixture pressure which is determined from the equation of state, τ_{ij} are the tensor components of viscous and turbulent stresses, E is the total energy of the gas mixture per mass unit, q_j are the vector components of the total heat flux, e_v is the vibrational energy of the gas mixture per mass unit, q_{vj} are the vector components of the total vibrational heat flux, and S_v is the vibrational energy source term.

Thus, the 3-dimensional solver is composed of ns+5 equations, except for the turbulence equations to be listed in Section 2.4. The density of the gas mixture is determined by the species concentrations:

$$\rho = \sum_{k=1}^{ns} \rho_k \tag{5}$$

$$Y_k = \rho_k / \rho \tag{6}$$

The Favre-averaged total energy E per mass unit of the mixture is composed of the internal energy, kinetic energy, and turbulent kinetic energy

$$E = \sum_{k=1}^{ns} Y_k e_k + \frac{u_j u_j}{2} + K \tag{7}$$

2.2. Transport properties

Here, transport properties refer to laminar transport and turbulent transport of momentum, energy (translational-rotational and vibrational) and species partial masses. The Boussinesq eddy viscosity assumption and a linear two-equation eddy viscosity model are adopted to account for the coupling of turbulence with vibration and chemistry.

Specifically, the vector components of the diffusion flux $J_{k,j}$, stress tensor deviator τ_{ij}, vector components of the total heat flux q_j, and vector components of the total vibrational heat flux $q_{v,j}$ are all contributed by both the laminar and turbulent parts:

$$J_{k,j} = \rho D_{L,k} \frac{\partial Y_k}{\partial x_i} + \frac{\mu_T}{\mathrm{Sc}_T} \frac{\partial Y_k}{\partial x_i} \tag{8}$$

$$\tau_{ij} = (\mu_L + \mu_T)\left[\left(\frac{\partial u_i}{\partial x_j} + \frac{\partial u_j}{\partial x_i}\right) - \frac{2}{3}\frac{\partial u_s}{\partial x_s}\delta_{ij}\right] \tag{9}$$

$$q_j = q_j^L + q_j^T \tag{10}$$

$$q_{v,j} = q_{v,j}^L + q_{v,j}^T \tag{11}$$

In Eq. (8), $D_{L,k}$ is the laminar diffusion coefficient of species k, μ_T is the turbulent eddy viscosity computed using the turbulence model, and Sc_T is the turbulent Schmidt number, which has a value of 0.9.

In Eq. (10) and Eq. (11), the laminar heat flux is calculated using two temperature gradients and mass diffusion as follows:

$$q_j^L = k_{tr}\frac{\partial T}{\partial x_j} + k_v \frac{\partial T_v}{\partial x_j} + \sum_{k=1}^{ns} \rho h_k D_k \frac{\partial Y_k}{\partial x_j} \tag{12}$$

$$q_{v,j}^L = k_v \frac{\partial T_v}{\partial x_j} + \sum_{k=mol} \rho e_{v,k} D_k \frac{\partial Y_k}{\partial x_j} \tag{13}$$

where k_{tr} is the thermal conductivity for transitional energy; and k_v is the thermal conductivity for vibrational energy. The laminar transport properties such as the viscosity and thermal conductivity for all species are obtained from the curve fits from the experimental results, and the Wilke's mixing rule is employed to compute the mixture's viscosity and thermal conductivity [11].

Similarly, the turbulent heat flux vector comprises high-order fluctuation terms, including contributions from translational temperature gradients, vibrational temperature gradients, and the mass diffusion, which cannot be neglected here:

$$q_j^T = \frac{\mu_T}{\mathrm{Pr}_T} Cp_{tr} \frac{\partial T}{\partial x_j} + \frac{\mu_T}{\mathrm{Pr}_T} Cp_v \frac{\partial T_v}{\partial x_j} + \frac{\mu_T}{\mathrm{Sc}_T} \tag{14}$$

$$q_{v,j}^T = \frac{\mu_T}{\mathrm{Pr}_T} Cp_v \frac{\partial T_v}{\partial x_j} \tag{15}$$

where a constant turbulent Prandtl number is assumed and the value of Pr_T is assumed to be 0.9 for evaluating the turbulent thermal conductivities.

2.3. Chemical reaction models

When computing the mass rate of production of certain species $\dot{\omega}_k$, we assume that the process of chemical reactions is unaffected by the turbulent fluctuations, namely the averaged production rate of chemical components is obtained by averaged temperature and averaged mass fraction of chemical components. The fluctuations terms in chemical reactions are neglected, which may produce nonphysical results in some cases of turbulent combustion, but such effects would be minimal as the flow in our study is strongly directional [31]. Hence, the interactions between chemical reactions and turbulence are beyond the scope of the current work.

Gupta's chemical reaction model [40] is adopted in our solver in which a finite set of complete chemical reactions with 11 species is considered in the chemical kinetics for dissociating or even ionizing air, including N_2, O_2, NO, NO^+, N_2^+, O_2^+, N^+, O^+, N, O, and e^-. Moreover, the specific details of this model can be found in Ref. [28]. Thus, the model used in our study can be further applied under conditions such as a higher Mach number considering the thermal ionization, which is superior to the commonly used 5-species model, including N_2, O_2, NO, N, and O [34]. Here, Park's two-temperature model is used in which the translational and rotational modes are characterized by the translational temperature (T), and the vibrational excitation of the diatomic species is characterized by the vibrational temperature (T_v). The rate of these reactions is decided by the two kinds of temperature.

2.4. Turbulence model

The current study uses the Menter's k-ω SST model [41,42], which keeps as the k-ω model inside the boundary layer and switches over to the k-ε model away from the surface.

$$\frac{\partial \rho K}{\partial t} + \frac{\partial}{\partial x_j}(\rho K u_j) = \mu_T \Omega^2 - \beta^* \rho K \omega + \frac{\partial}{\partial x_j}\left[(\mu_L + \sigma_k \mu_T)\frac{\partial K}{\partial x_j}\right] \tag{16}$$

$$\frac{\partial \rho \omega}{\partial t} + \frac{\partial}{\partial x_j}(\rho \omega u_j) = \gamma \rho \Omega^2 - \beta \rho \omega^2 + \frac{\partial}{\partial x_j}\left[(\mu_L + \sigma_\omega \mu_T)\frac{\partial \omega}{\partial x_j}\right] + 2(1-F_1)\rho \sigma_{\omega 2}\frac{1}{\omega}\frac{\partial K}{\partial x_j}\frac{\partial \omega}{\partial x_j} \tag{17}$$

The turbulent viscosity can be expressed as

$$\mu_T = \min\left[\frac{\rho K}{\omega}, \frac{a_1 \rho K}{F_2 \Omega}\right] \tag{18}$$

where Ω is the magnitude of vorticity. All the constants used in the SST model are blended from the corresponding constants of the k-ε and the k-ω models via $\varphi = F_1\varphi_1 + (1 - F_1)\varphi_2$.

And the F_1 term is given by:

$$F_1 = \tanh\left\{\left\{\min\left[\max\left(\frac{500\mu_L}{\rho\omega\, d^2}, \frac{\sqrt{K}}{0.09\omega d}\right), \frac{4\sigma_{\omega 2}\rho K}{d^2 CD_{k-\omega}}\right]\right\}^4\right\} \tag{19}$$

with $CD_{k-\omega} = \max\left(\rho\frac{2\sigma_{\omega 2}}{\omega}\frac{\partial K}{\partial x_j}\frac{\partial \omega}{\partial x_j},\ 1\times 10^{-20}\right)$ and d is the distance to the nearest wall. The F_2 term is given by:

$$F_2 = \tanh\left[\left[\max\left(\frac{500\mu_L}{\rho\omega\, d^2}, \frac{2\sqrt{K}}{0.09\omega d}\right)\right]^2\right] \tag{20}$$

The constants for the present model are $\beta^* = 0.09$, $a_1 = 0.31$,

Table 1
Freestream conditions for hypersonic cylinder flow.

Parameters	Experiment	Computation
Test gas	Air	Air
p_∞ [Pa]	476	488.8
T_∞ [K]	901	910
ρ_∞ [kg/m^3]	1.547×10^{-3}	1.55×10^{-3}
Ma_∞	8.98	8.76
U_∞ [m/s]	5956	5956

2.5. Numerical methods

$\gamma_1 = 5/9,\ \gamma_2 = 0.44,\ \beta_1 = 0.075,\ \beta_2 = 0.0828,\ \sigma_{k1} = 0.85,\ \sigma_{k2} = 1.0,\ \sigma_{\omega1} = 0.5,\ \sigma_{\omega2} = 0.856.$

This solver is based on the structured multi-block mesh and finite difference method. The AUSMPW+ [43] second order upwind scheme with MUSCL reconstruction is used for inviscid fluxes. Fully catalytic, partially catalytic and non-catalytic wall conditions are all included in this solver [44]. The no-slip isothermal wall is set to be the wall-boundary condition according to the experimental conditions chosen in the current study. The time discretization is solved using the lower-upper symmetric Gauss–Seidel implicit time integration method. Specifically, to solve the rigidity problem brought by the thermochemical source terms, the present solver adopts an implicit treatment for the non-viscous term, the source term as well as an implicit treatment for the viscous term. The codes can be executed in parallel by means of a message-passing interface system. Uniform flow is used to initialize the flow field, and the calculation converges when the total residual has declined more than four orders of magnitude.

3. Code validation

3.1. Hypersonic laminar flow of the cylinder at high-enthalpy conditions

The hypersonic cylinder experiment conducted at the high-enthalpy shock tunnel of the German Aerospace Center by Karl et al. [45] was selected as a case to validate our code's capability in simulating hypersonic TCNE flow. The cylindrical model was equipped with 17 pressure transducers and the same number of thermocouples to measure surface pressure and heat flux data. The freestream conditions in the computation were selected from Gaitonde's [46] simulation, as shown in Table 1. The inflow gas was air, and the measured total enthalpy was 22.4 MJ/kg. Under these circumstances, the non-equilibrium thermochemical relaxation processes in the shock layer were significant enough to alter the flow-field parameter distribution and the shock standoff distance. Additionally, the wall boundary was assumed to be fully catalytic with a fixed temperature of 300 K, and the radiation was ignored in the calculation. The domain for this cylinder case was 119 × 99 in the normal and streamwise directions, respectively. Clustering near the wall was implemented, and the first layer mesh height was 2×10^{-6}.

Fig. 2 shows the heat flux and pressure distributions along the surface of the cylinder. It can be seen that both the pressure and heat flux distributions obtained in this work are in good agreement with the experimental data. Moreover, compared with Gaitonde's [46] simulation results, the heat flux distribution is observed to be closer to the experiment, although the peak value was underpredicted by ~3%, validating the code's ability to simulate TCNE flows. From the analysis

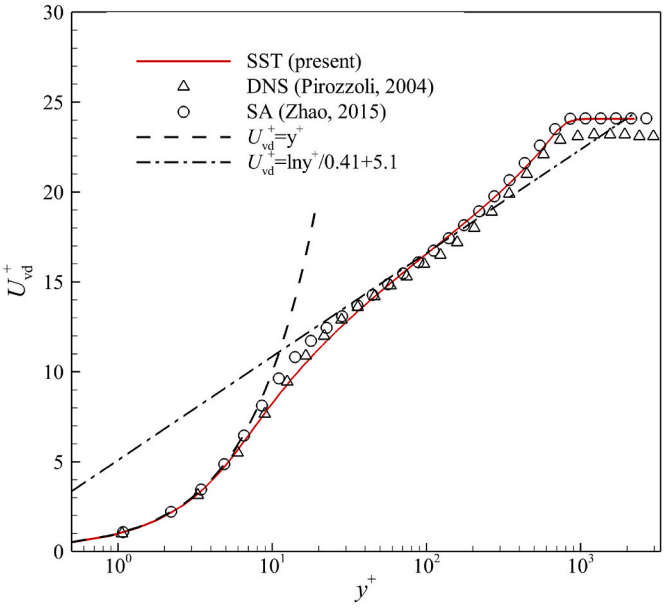

Fig. 3. Comparison of turbulent velocity profiles with log laws and reference data [49,50].

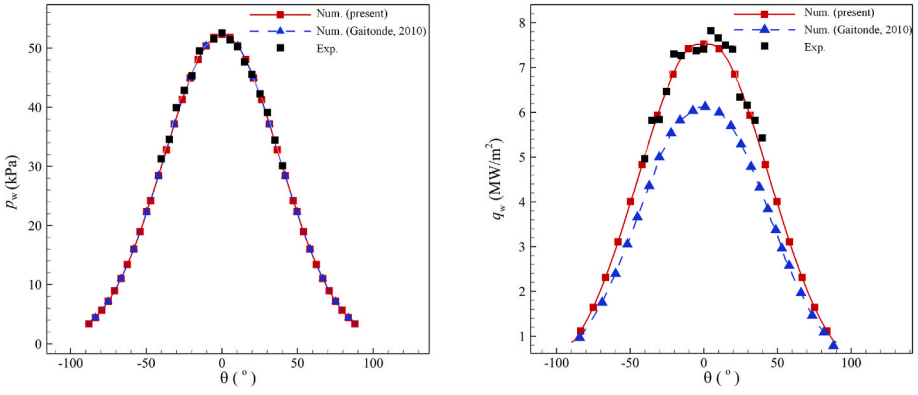

(a) Wall pressure (b) Heat flux

Fig. 2. Pressure and heat flux distributions along the surface of the cylinder.

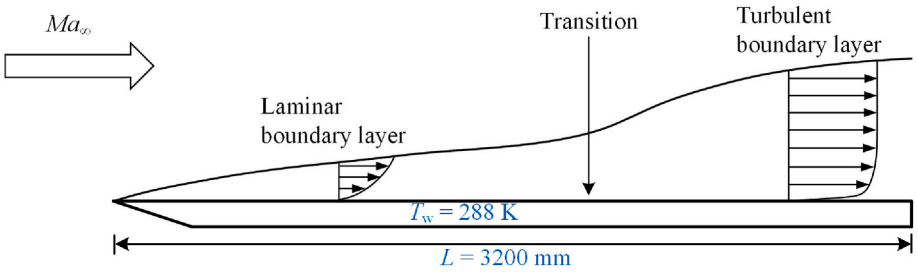

Fig. 4. Configuration of hypersonic transition of the flat-plate.

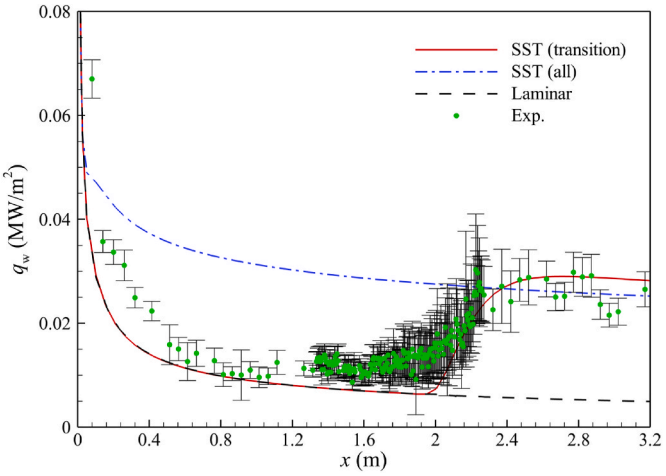

Fig. 5. Comparison of wall heat flux between experiment data and numerical results (forced transition, turbulent and laminar cases) in *Ma*7 transition.

in Ref. [46], the heat flux is much affected by the boundary condition, in which fully catalytic boundary conditions yield better results than partially catalytic or non-catalytic solutions. While the surface pressure is unaffected by the boundary condition and is very accurately predicted.

Moreover, another hypersonic laminar validation case was conducted in our previous study [47]; we chose the flight experiment conditions of the Orbital Reentry Experiment capsule at a higher Mach number than 15. Specifically, the computation conditions corresponded to the flight conditions at $H = 59.6$ km, $Ma = 17.61$ and $T_w = 1519$ K. A finite-rate catalytic model with a fixed recombination coefficient of 5.0×10^{-3} was also used for aerothermal simulations. It was shown that the heat fluxes obtained by our solver is in good agreement with Fujino's computational results [48].

3.2. Supersonic turbulent flow of the flat-plate

We computed the $Ma = 2.25$ turbulent boundary layer profile of the flat-plate flow field using the SST turbulence model. DNS data of the compressible boundary layer from Pirozzoli et al. [49], Spalat–Allmaras (SA) turbulence model data from Zhao [50], and the van Driest law of the wall were taken as references, as shown in Fig. 3. Computational results were coincident with reference data and theory. It is clear that the van Driest transformation of the velocity from the SST results exceeded 21 when $y^+ > 400$, demonstrating a fully turbulent boundary layer [35].

The non-dimensional parameters in the van Driest transformation are as follows:

$$y^+ = \frac{\rho_w u_\tau y}{\mu_w} \tag{21}$$

$$u^+ = \frac{u}{u_\tau} \tag{22}$$

$$u^+_{VD} = \int_0^{u^+} \left(\frac{\rho}{\rho_w}\right)^{1/2} \mathrm{d}u^+ \tag{23}$$

where ρ_w is the wall density, μ_w is the wall viscosity, μ_τ is the friction velocity, and u^+_{VD} is the van Driest transformed velocity.

3.3. Hypersonic transition of the flat-plate

The third case is the $Ma = 7$ hypersonic transition experiment recently conducted by Liu [51] in the JF-12 shock tunnel of the Institute of Mechanics, Chinese Academy of Sciences. This shock tunnel is operated with a 268-m-long backward detonation driver and a 2.5-m-long nozzle, which is capable of reproducing hypersonic flight conditions from $Ma = 5$–9 at altitudes of 25–50 km. The total available test time of this tunnel is approximately 130 ms.

A basic illustration of the hypersonic natural transition is shown in Fig. 4. The length and width of the flat-plate made of stainless steel is 3.2 m and 1.2 m, respectively, and the inflow conditions are $Ma_\infty = 7.0$, $Re/\mathrm{m} = 1.23 \times 10^6$, $T_\infty = 205.56$ K, and $T_w = 288$ K. In this experiment, coaxial thermocouple sensors are used to measure the wall heat flux and are placed every 5 mm streamwise between $x = 1.333$ m and $x = 2.267$ m in order to capture the precise changes in heat flux data during the transition. Meanwhile, in other regions, the sensors are arranged

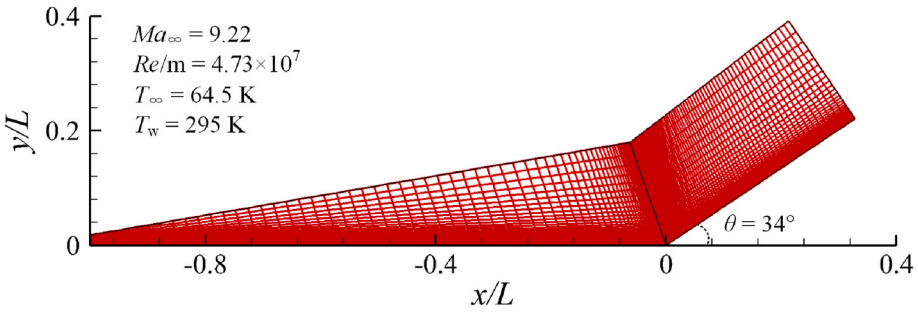

Fig. 6. Grid of 34°compression corner in low-enthalpy case.

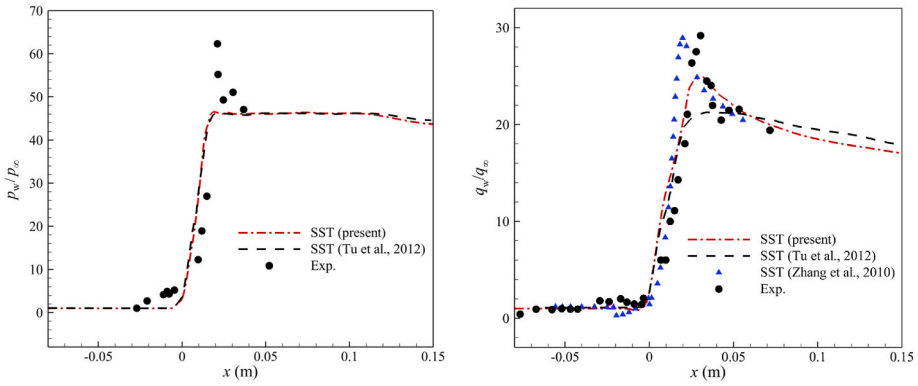

(a) Normalized wall pressure (b) Normalized heat flux

Fig. 7. Results of 34° compression corner by SST turbulence model.

relatively sparsely: every 50 mm streamwise. This type of sensor is small in size, resistant to erosion, and has excellent performance under transient high heat flow conditions with a relative measurement error of less than 2%. As shown in Fig. 5, the transition starts at about $Re_x = 2.60 \times 10^6$ because the heat flux data measured on the wall rise approximately at this point [51]. The thermocouple data (sampled at 200 kHz) are averaged over a comparatively large time window of total 100 ms. The error bars shown on the figures represent the standard deviation of the signal from this average in the window. The unsteadiness of the signal during the transition process is implied by larger error bars.

In our computations, laminar, forced transitional, and turbulent cases with the SST turbulence model were compared to the experimental results. In the laminar region, laminar and transitional cases slightly underestimated the heat flux because the modeling of the front edge cannot be guaranteed the same as the experiment configuration. Although the turbulent and transitional models provided satisfactory results that fall inside the experimental data range in the turbulent region, the latter is lower than the former with an increasing height of boundary layer. Hence, the heat flux prediction of the flat-plate is quite acceptable using the present SST model.

3.4. Hypersonic shock wave/turbulent boundary interaction on the compression corner at low-enthalpy conditions

The hypersonic experiment for a $Ma = 9.22$ flow over a 2D compression corner by Coleman [52] is a canonical source for testing turbulence models from which acceptable wall data were measured. The 34° hypersonic compression corner shown in Fig. 6 was selected for this test case, and the freestream conditions are listed. Owing to the low temperature of inflow, the level of total enthalpy was comparatively low and computations were in the range of a calorically perfect gas. The dimensions of the solution domain for the compression corner were 141 × 81 in the x and y directions, respectively. The length of plat-plate was set to 0.56 m, which is the same as that in Tu et al. [53] and Zhang et al. [54]. Clustering near the wall and the leading edge was implemented, and the first layer mesh height was 1×10^{-6} to ensure that $y^+ < 1$.

Fig. 7 presents the comparisons of normalized wall pressure and heat flux between present SST results and the reference results [53,54]. Notably, the results from Tu were of the second-order scheme used to maintain consistency with the present solver. In Fig. 7 (a), the results of normalized wall pressure by our solver matched well with Tu's results using the same turbulence model. However, the SST turbulence model of our solver and Tu's all underestimated the length of separation and the overshoot of pressure measured after the corner point. Meanwhile, the results of heat flux in Fig. 7 (b) show a large difference. The peak heat flux predicted by Tu was much lower than the experimental data, whereas the rising slope by Zhang was larger, leading to a misleading position of peak heat flux. The present solver can capture the right position of peak heat flux, although the peak value lay between those of Tu and Zhang. Moreover, the uncertainty in closure coefficients, different schemes, and mesh refinements might bring about discrepancies in shock wave/boundary layer interaction simulations that use turbulence models.

From the test cases above, although there were discrepancies between the experimental results and the computations, it is believed that the current TCNE gas model coupled with the turbulence model has demonstrated notable improvements to the heating prediction.

Table 2
Freestream conditions for compression corner.

Conditions at flight height of 30 km			
T_∞ [K]	226.51	Ma_∞	20
ρ_∞ [kg/m^3]	1.84×10^{-2}	U_∞ [m/s]	6034.17
T_w [K]	1500	Re/m	7.53×10^6

Table 3
Grids used in the sensitivity study.

Grid	$i \times j$	Wall distance of first layer mesh/μm	Maximum deviation of wall pressure/%	Maximum deviation of wall heat flux/%
Coarse	121 × 81	5	3.07	19.22
Medium	251 × 121	1	0	0
Fine	381 × 161	0.5	1.72	3.83

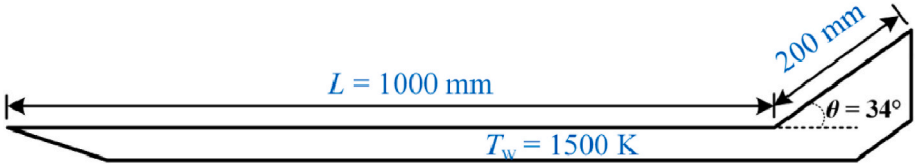

Fig. 8. Configuration of 34° compression corner at flight height of 30 km.

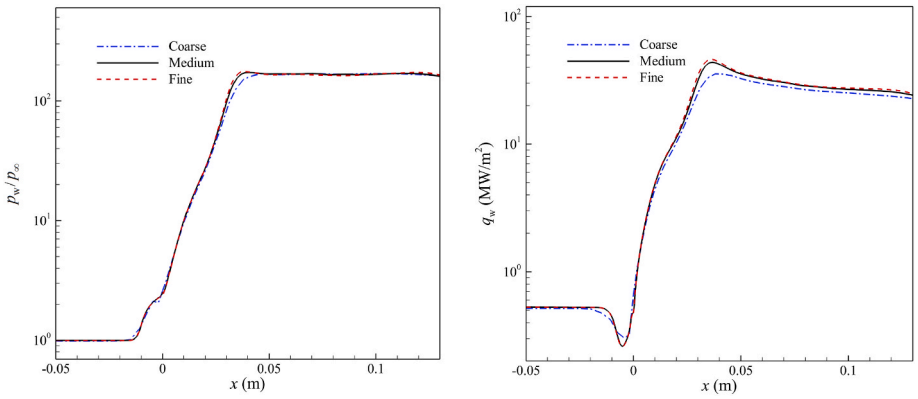

(a) Normalized wall pressure (b) Heat flux

Fig. 9. Grid sensitivity of normalized wall pressure and heat flux.

4. Computational details

4.1. Calculation conditions

A compression corner is a typical configuration that induces shock wave/boundary layer interactions in different parts of hypersonic vehicles (e.g., scramjet intakes and control surfaces). Under critical altitudes and speeds, the presence of the transition to turbulence with the TCNE effect often leads to large modifications of pressure and heat flux distributions, which spoil aerodynamic efficiency and thermal protection system margins.

With this background, the 34° compression corner with a 1000-mm long upstream flat-plate was selected as the research object, and Fig. 8 presents a sketch. The upstream plat-plate satisfies the full turbulence assumption with the forced transition trip. Regarding the boundary conditions, we used the non-reflecting conditions at the far-field and the non-slip conditions at the wall. The wall temperature was selected at 1500 K as a result of a long-time endurance at high speeds. Ablation is not considered for purposes of obtaining a more basic understanding of the shock wave/boundary layer interaction phenomena, and it is desirable to obtain direct data in the absence of mass transfer. The design point at $H = 30$ km cruise altitude with a zero angle of attack and varying Mach numbers of 10, 15, and 20 is considered. A comparative study on the laminar and turbulent boundary layer conditions was considered at $Ma = 20$, and the freestream conditions of the cases are listed in Table 2.

4.2. Grid sensitivity study

A grid refinement study was conducted to confirm that the solution is grid-independent. The grid distributions used are shown in Table 3. We studied three sets. The computational domain was discretized using 121 × 81, 251 × 121, and 381 × 161 (wall normal × streamwise) points with a first-layer height of 5×10^{-6}, 1×10^{-6}, and 0.5×10^{-6} m, respectively. The bi-exponential stretching law as applied along the streamwise direction, and the hyperbolic stretching law was applied along the wall-normal direction for clustered distributions at the leading edge, corner point, and wall.

The distributions of pressure and heat flux on the wall for the three sets of grids are plotted in Fig. 9. The plotted curves show little difference in the maximum pressure and heat flux between the medium and fine grids and a larger difference between the coarse and medium grids. The maximum deviation of the fine mesh from the medium mesh for the pressure was about 1.72%, and the maximum deviation in the heat flux was about 3.83%, whereas the corresponding deviations between the coarse and medium mesh were 3.07% and 19.22%, respectively. It can be seen that the results of the last two grids in Table 3 are almost identical. The medium grid is therefore deemed sufficient to produce grid converged solutions and is chosen for our further study.

4.3. Accumulation of error

Estimation of numerical errors is necessary to characterize the reliability of the numerical results. According to Smirnov et al. [55], systematic error and stochastic error are two sources of numerical errors in the simulations. The systematic error is often caused by the defective algorithm or physical model and can be identified through the code validation and verification process. The stochastic error is closely related to poor spatial resolution and low accuracy of temporal integration. Smirnov et al. [56] showed that the numerical error could accumulate with time if the stochastic error is large in the unsteady flow simulations. The relative error of integration is proportional to the mean ratio of cell size and scheme accuracy, and specific definitions can be found in Refs. [55,56].

A ratio expressed by R_s is used to characterize the accumulated error, as shown in Eq. (24). A higher value of R_s signifies a lower error, and the error tends to the maximal allowable value if R_s tends to unity.

$$R_s = n_{\max}/n \tag{24}$$

where $n_{\max}$ is the maximal allowable number of time steps for the numerical solution, and n is the number of time steps.

The detailed data of precision estimation are provided in Table 4. From the table, it can be seen that with the convergent grid and numerical methods presented above, the calculated value of R_s is well above unity, indicating a significantly low error.

Table 4
Numerical calculation error estimates.

Allowable error	Grid resolution	Number of iterations (n)	Accumulated error	Allowable number of time steps ($n_{\max}$)	Reliability $Rs = n_{\max}/n$
5%	121 × 81	80,000	$2.446 \cdot 10^{-6}$	$4.179 \cdot 10^{8}$	5224
5%	251 × 121	150,000	$6.277 \cdot 10^{-7}$	$6.345 \cdot 10^{9}$	$4.23 \cdot 10^{4}$
5%	381 × 161	210,000	$2.577 \cdot 10^{-7}$	$3.765 \cdot 10^{10}$	$1.793 \cdot 10^{5}$

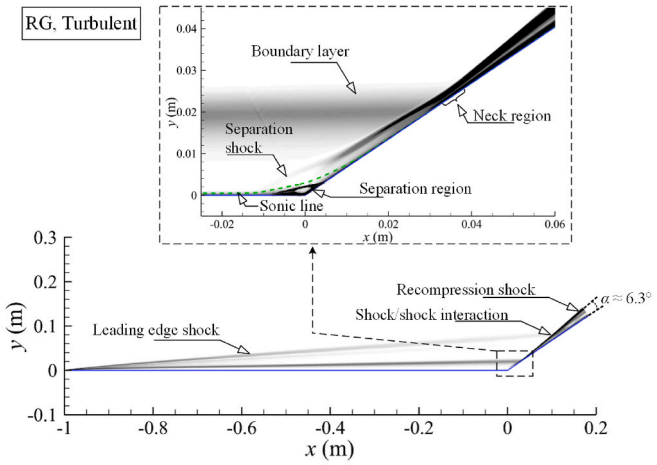

(a) Real gas, turbulent case

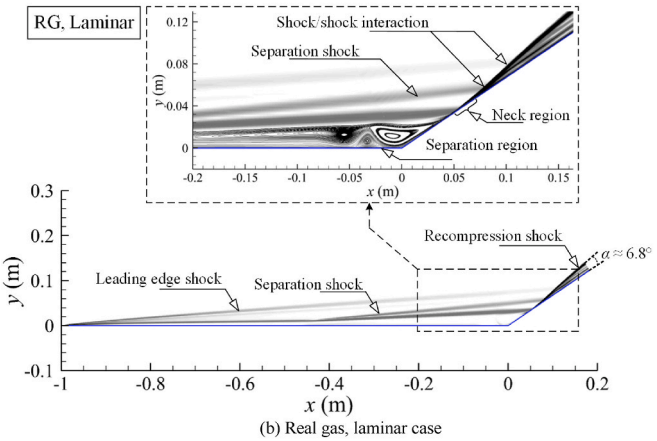

(b) Real gas, laminar case

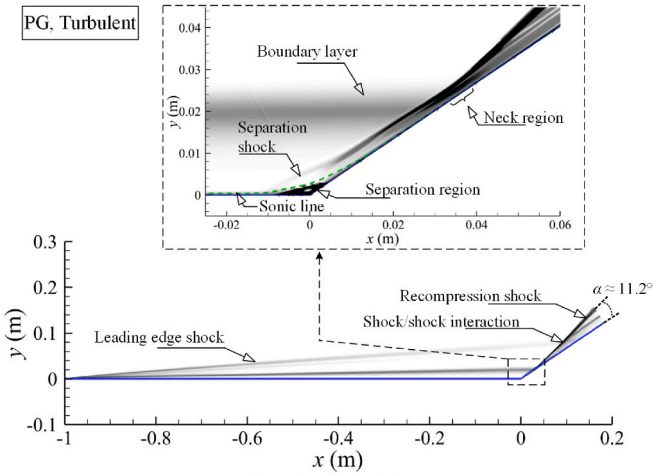

(c) Perfect gas, turbulent case

Fig. 10. Density gradient contours of 34° compression corner with three models.

5. Results and discussion

5.1. Flow-field comparison

To assess the importance of turbulence and TCNE, we carried out simulations using different gas models. Detailed computation descriptions are listed in Table 2. We first compared flow visualizations by means of density-gradient contours of the real gas turbulent case, the real gas laminar case, and the perfect gas turbulent case in Fig. 10 with an enlarged view of the corner region.

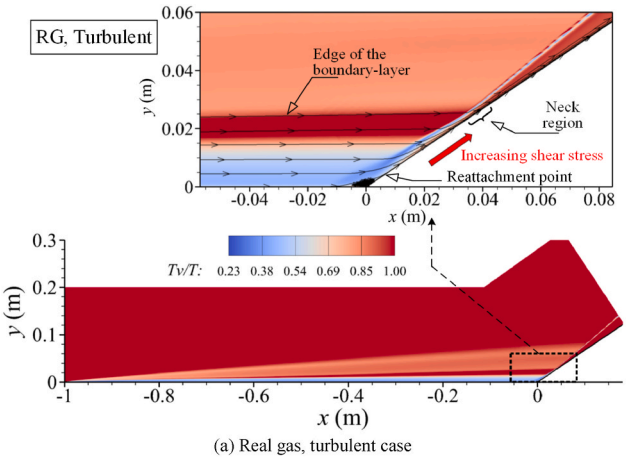

(a) Real gas, turbulent case

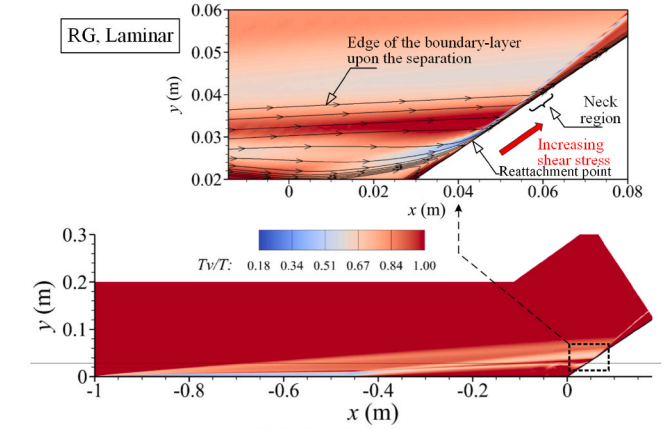

(b) Real gas, laminar case

Fig. 11. Contours of the ratio of vibrational to translational temperature, Tv/T, in two real gas cases.

The basic structures of the three flow fields are clearly displayed in Fig. 10. The three cases share the same major features in the flow field, which contain the leading-edge shock, separation shock, recompression shock, shock/shock interaction as well as vortices (annotated by streamlines) in the separation region. In our research, the leading edge of the plate was set sharply to exclude the entropy-layer effect, although most hypersonic vehicles' noses are blunt. Thus, a leading-edge shock formed at the front of the plate and hit the recompression shock where the x-direction position is approximately 0.12 m in the three cases. Beyond the general flow features of shock wave/boundary layer interaction, however, the TCNE and turbulence effects may cause several consequences, as discussed next.

The most prominent characteristic feature is a small separation region in the presence of turbulence. It is well-known that the pressure rise caused by the deflection of flow at the corner induces the separation region. The separation length is dictated by the ability of the shear layer to overcome the adverse pressure rise from the origin at the separation point to the reattachment point. The separation length is barely affected by the TCNE because the lengths in cases (a) and (c) are almost the same. Specifically, the two types of incoming boundary-layer conditions make a big difference to the separation length: this is ~507 mm for the laminar case, indicating a large separation, and ~14 mm for the turbulent case, indicating a small separation. Moreover, the feature of the green sonic line reveals the reason for the formation of a weaker interactive response of the incoming turbulent boundary layer: the sonic line

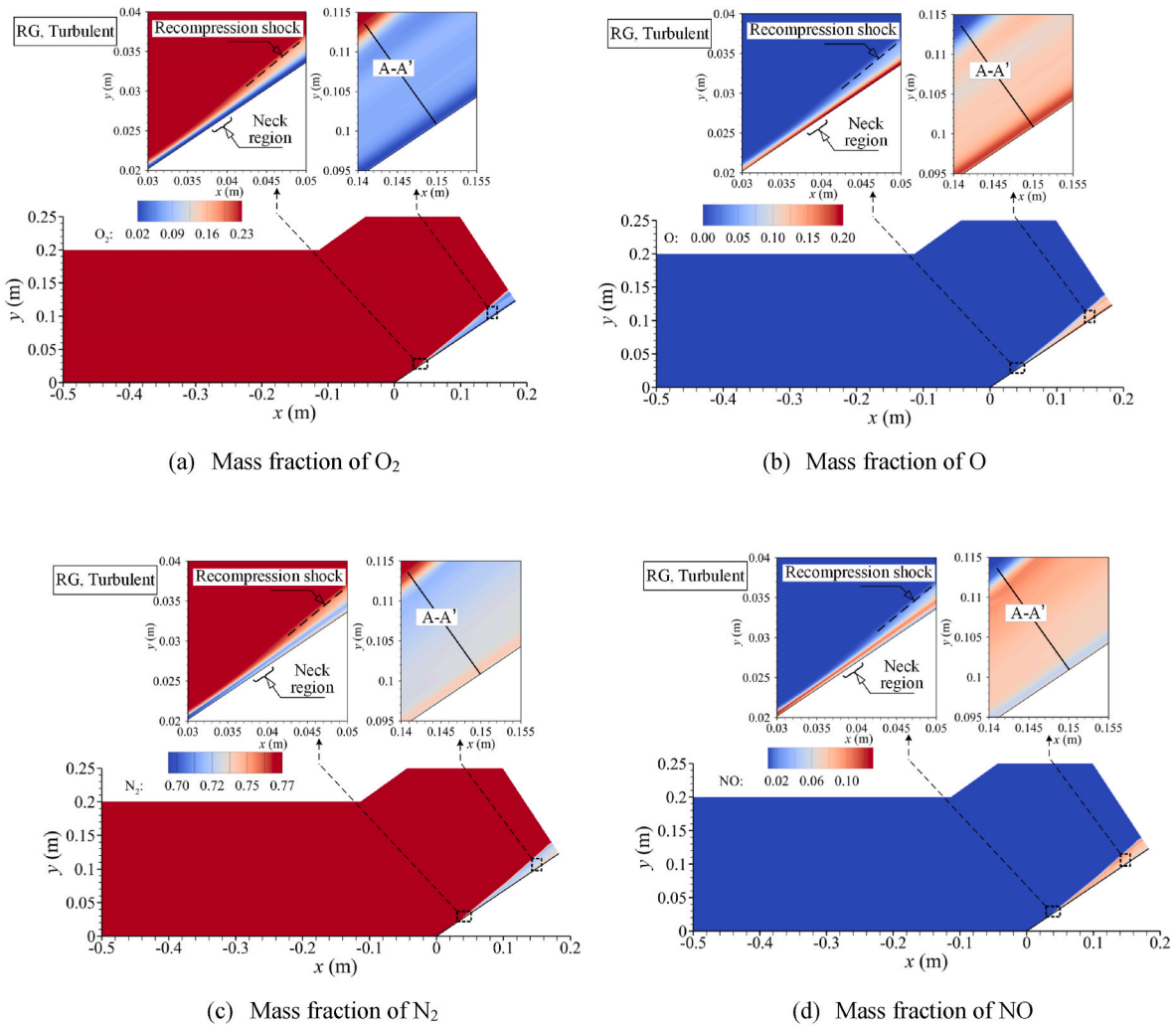

(a) Mass fraction of O_2 (b) Mass fraction of O

(c) Mass fraction of N_2 (d) Mass fraction of NO

Fig. 12. Species mass fractions for the real gas, turbulent case. A-A′, wall normal at the $x = 0.15$ m.

lies deep within the turbulent layer (i.e., typical values of y_{sonic}/δ are less than 0.01). The velocity profile is far fuller than that of a laminar boundary layer. The existence of secondary eddies embedded within the separation region in the laminar case is also remarkable, which agrees with other hypersonic shock wave/laminar boundary layer interaction simulations at large corner angles [16,57].

A second characteristic feature is the steep separation shock embedded deep inside the boundary layer in the turbulent cases. For those cases in real and perfect gases, the compression waves around the separation and reattachment points coalesce rapidly to produce steep shock waves from the sonic line inside the boundary layer. On the contrary, for the laminar case, the separation shock starts much earlier because of the large separation and hits the recompression shock at the triple-point.

A third characteristic feature is the different location of the neck region. Generally, the neck region forms at the thinnest part of the streamline tube after streamlines turn towards the surface, and it is located between the reattachment point and recompression shock [21]. For turbulent cases, the neck region seems closest to the edge of the boundary-layer, whereas the neck region in the laminar flow is lifted by a large separation in the vicinity of the boundary-layer edge. The location of the neck region is our main focus, owing to its special physical meaning, which is discussed later. Moreover, the formation of the neck region is more prominent with the real gas compared with the perfect gas.

Another characteristic feature is the small recompression shock angle in the TCNE case, which is defined as the angle between the recompression shock and the ramp, noted as α. The comparisons show that major differences exist in the recompression shock angle, α, between the three sets of simulation results. Specifically, the recompression shock angle, α, in the RG turbulent case is 6.3°, which is almost half that in the PG turbulent case (11.2°); it is approximately the same as that in the RG laminar case (6.8°). This phenomenon can be illustrated by an analogy with hypersonic computations of a blunt body [58], in which the bow shock stand-off distance is much larger when using perfect gas than when using real gas. The reactions taking place behind the bow shock absorb much heat and alter the density field significantly afterward.

5.2. *Effect of thermochemical non-equilibrium*

In this section, the thermal and chemical non-equilibrium are discussed respectively for the RG turbulent case and the RG laminar case.

Fig. 11 shows the ratio of the vibrational to translational temperature (Tv/T) over the 34° compression corner with an enlarged view of the neck region. This serves as an indication of the degree of thermal nonequilibrium in the flow. For both cases, the inviscid region is nearly in thermal equilibrium. In the boundary layer upstream of the separation, the vibration is marginally excited, where $Tv/T \approx 0.25$, and the viscous-dominant flow remains thermally frozen. Across the leading-edge shock and recompression shock in both cases, and the separation shock in the laminar case, a further increase in translational temperature is evident, where $Tv/T \approx 0.6$. Remarkably, the recompression shock is

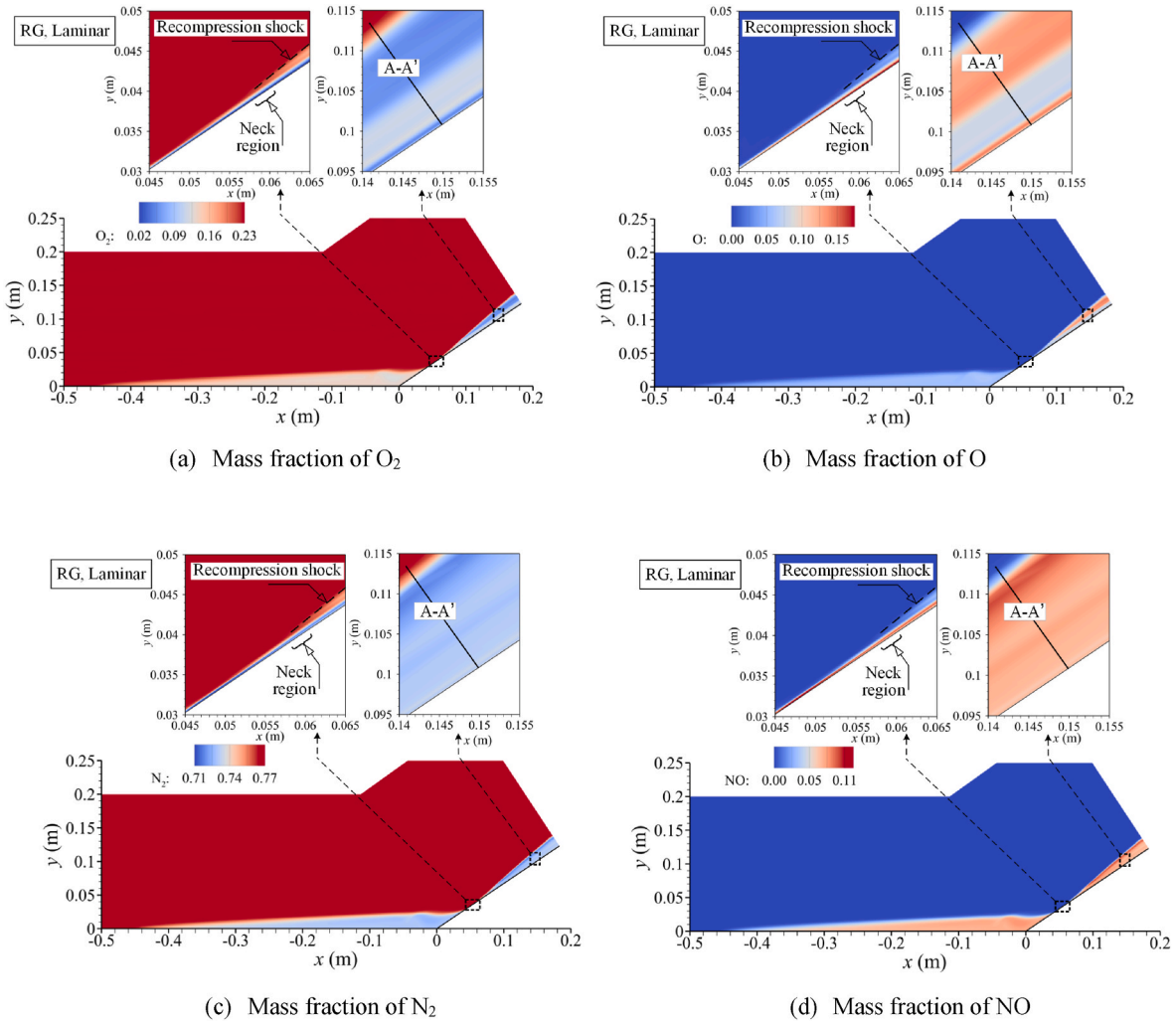

Fig. 13. Species mass fractions for the real gas, laminar case. A-A′, wall normal at the $x = 0.15$ m.

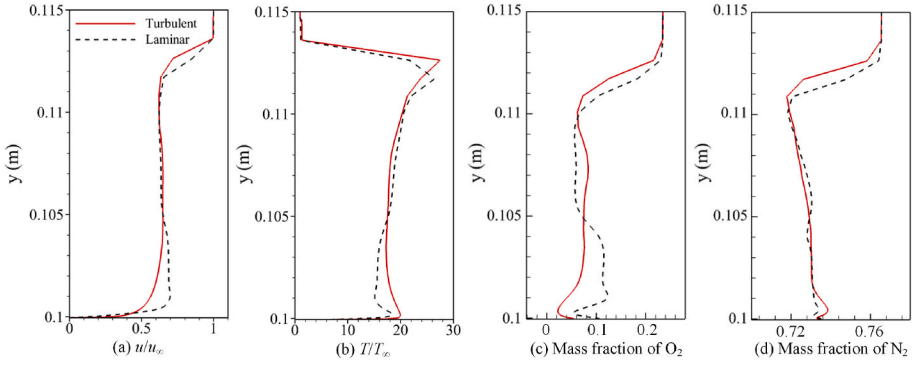

Fig. 14. Profiles of section A-A' (see Figs. 12 and 13): (a) Velocity; (b) Temperature; (c) Mass fraction of O_2; and (d) Mass fraction of N_2.

clearly visualized by this ratio as the flow quickly recovers thermal equilibrium after the shock. Within the separation bubbles in the laminar case, a large region exists, suggesting that the flow approaches thermal equilibrium. Moreover, from the reattachment point to the neck region, the wall shear stress increases in both cases as the flow accelerates to the edge of the boundary layer.

Fig. 12 shows species mass fractions for the RG turbulent case. Reactions merely occur on the flat-plate, and much of O_2 dissociates behind the recompression shock, which is consistent with the increase of O in the same region. Although the dissociation of N_2 is not as strong as O_2, it is interesting to note that there is an increase of N_2 and a reduction of NO near the wall of the ramp.

Fig. 13 shows species mass fractions for the RG laminar case. Reactions are seen within the separation region, where the species are nearly frozen. Dissociation of O_2 and formation of O, as can be seen, are highest behind the recompression shock and the near-wall shear layer downstream of reattachment. The distributions of N_2 and NO are much more uniform after the recompression shock than that of the RG

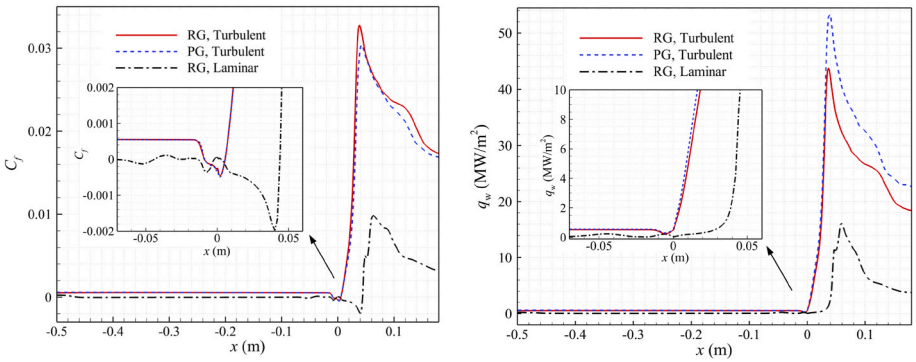

(a) Skin friction distributions (b) Heat flux distributions

Fig. 15. Comparisons of wall data distributions among the three cases (real gas turbulent, perfect gas turbulent, and real gas laminar).

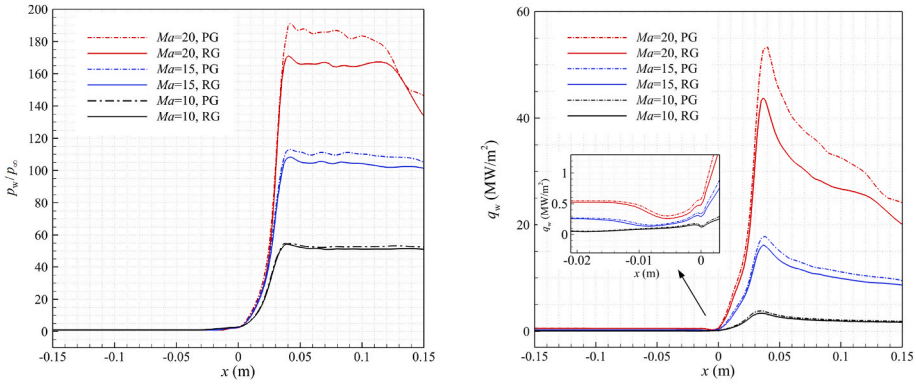

(a) Normalized wall pressure distributions (b) Heat-flux distributions

Fig. 16. Effect of Mach number between perfect gas turbulent and real gas turbulent cases.

turbulent case.

Fig. 14 shows the profiles of streamwise velocity, temperature, and mass fractions of O_2 and N_2 at section A-A' between the RG turbulent and RG laminar cases, where u and T are normalized by their corresponding freestream values. By first considering the velocity profile in Fig. 14(a), the thickness of the turbulent boundary layer on the ramp is larger than the laminar one. The flow velocity in the two cases at the after-shock region ($y \approx 0.105$ to $y \approx 0.111$) is nearly the same, owing to the subequal recompression shock angles. As seen in Fig. 14(b), there are two peaks of temperature at the compression shock and near the wall in both cases. However, the temperature gradient for the turbulent case at the surface is far more significant. Considering the mass fraction of O_2 and N_2 in Fig. 14(c) and (d), dissociation of the molecules occurs after the shock. Additional reduction of O_2 is consistent with the temperature jump inside the boundary layer, where some recombination of N_2 is also seen, especially in the RG turbulent case.

5.3. Wall data distributions

The distributions of skin friction along the wall among the three cases are shown in Fig. 15(a). As can be seen, the difference between the RG turbulent and PG turbulent cases is minimal on the plate, but farther away from the corner, this difference becomes indistinguishable on the ramp. This implies that the TCNE effect increases the skin friction of STBLI, which agrees with reported laminar simulations [30]. This may provide further guidance to aerodynamic design. Moreover, the skin friction in the RG laminar case is lower than that in the RG turbulent case both on plate and ramp, of which the peak value lies in the neck region, reaching about 1/3 of the one in RG turbulent case.

Fig. 15(b) presents the heat flux data. As with the distributions of skin friction, the heat flux is slightly affected by the thermal non-equilibrium on the turbulent boundary-layer of the flat-plate before separation. Then, the heat flux of the turbulent case experiences a slight drop, indicating an incipient separation, after which it comes to the neck region. The difference of the heat flux on the ramp between the RG

Table 5
Maximum wall data in perfect gas turbulent and real gas turbulent cases under different Mach numbers.

	Maximum normalized wall pressure		Maximum wall heat flux (MW/m^2)		Maximum deviation of wall pressure/%	Maximum deviation of wall heat flux/%
	Perfect gas, turbulent	Real gas, turbulent	Perfect gas, turbulent	Real gas, turbulent		
Ma = 10	54.67	54.26	3.80	3.37	0.75	11.32
Ma = 15	113.03	108.32	17.73	16.15	4.17	8.91
Ma = 20	191.28	170.92	53.28	43.76	10.65	17.87

turbulent and PG turbulent cases is quite large, indicating that TCNE has a strong effect on the heat flux of STBLI. In the laminar case, the data fluctuate slightly inside the separation region due to the vortex pairs, which agrees with the hypersonic strong/weak viscous-interaction theory [16]. Two peaks then exist, running from the reattachment point to the neck region as illustrated in Fig. 11. Regarding the peak value of heat flux in real gas, it is important to judge the boundary-layer conditions before the interaction region because there could be a significant difference in which the value is 16.0 MW/m^2 in the RG laminar case and 43.8 MW/m^2 in the RG turbulent case (about 2.74 × the laminar level). Another noteworthy feature in all cases is that the heat flux decreases because of the attenuation of the compression effect and drops inhomogeneously because of expansion waves from the triple-point.

5.4. Effect of Mach number

To evaluate the extent to which the TCNE affects the STBLI at a wide range of Mach numbers, all parameters are kept constant other than Ma = 10, 15, and 20. Comparisons are made between models using PG turbulent and RG turbulent gases in these cases. Meanwhile, by increasing the Mach number, the local enthalpy in the flow field increases.

Fig. 16(a) provides a comparison of normalized wall-pressure distributions for different Mach numbers. For higher Mach numbers, the pressure upstream rises more closely at the corner, leading to a reduction in size of the separation region. Additional peak pressures are reached at their neck regions and remain as a plateau until the intersection of expansion waves on the wall drop. The pressure after the neck region on the ramp is greatly affected by the TCNE in the $Ma = 20$ case, but it is marginally affected when $Ma = 10$. Meanwhile, it is observed that this effect is analogous to the heat flux distributions, as shown in Fig. 16(b). As the Mach number increases, the discrepancies between heat flux distributions of the ramp in the PG and RG case increase.

Table 5 shows the detailed comparisons of peak data for all cases. The maximum deviation of wall pressure between PG turbulent and RG turbulent cases rises with respect to higher Mach numbers, in which the effect can be ignored when $Ma = 10$, whereas it can be as high as 10.65% when $Ma = 20$. However, there are larger deviations in terms of maximum heat flux. Even at $Ma = 10$, the deviation of the prediction using two models can be as high as 11.32%, reaching its maximum at $Ma = 20$ (17.87%). Furthermore, the maximum heating levels generated in the neck region for the RG turbulent case and the Mach number can be correlated approximately in terms of a simple power-law relationship: $q_{w_max} \propto Ma^{11/3}$.

6. Conclusions

For a high Mach number (>10) flight in the relatively lower layers of near-space, the influence of thermal and chemical nonequilibrium phenomena on shock wave/turbulent boundary-layer interactions induced by the compression corner in a hypersonic vehicle was studied in this paper. The main conclusions are stated as follows:

(1) Traditional SST turbulence model that couples hypersonic flows in calorically perfect gas model was transformed and implanted into the hypersonic flow solver in a thermochemical non-equilibrium (real gas) model. Our novel solver was carefully validated using a series of test cases, including laminar cylinder flow at a high-enthalpy condition, a supersonic turbulent flat-plate, the hypersonic transition of a flat-plate, and hypersonic shock wave/turbulent boundary-layer interaction at a low-enthalpy condition. Results show that the solver has a good prediction capability regarding turbulent and thermochemical non-equilibrium flows.

(2) The 34° corner flow at flight conditions of a Mach number of 20 and a height of 30 km was studied to investigate the coupling effects of thermochemical non-equilibrium and turbulence on local parts of hypersonic vehicles (e.g., control surfaces) by using three types of gas models (i.e., real gas with turbulence, perfect gas with turbulence, and real gas without turbulence). Results show that the flow properties of the compression corner differed considerably when the thermochemical non-equilibrium and turbulence were considered. The presence of the turbulent boundary layer greatly reduced the size of the separation zone and changed the flow-field organization. Notably, the mechanisms of the neck region accompanying the maximum heat flux, the wall pressure, and the skin friction in both laminar and turbulent cases were well-interpreted, for which it was found that the position should accounted for during the design process.

(3) The thermochemical non-equilibrium had a little effect on the separation length of shock wave/turbulent boundary-layer interaction and the wall data on the flat-plate, but it greatly reduced the recompression shock angle, the wall pressure, and the heat flux on the ramp; it also slightly increased the friction at Mach number 20. Hence, it is necessary to consider both thermal and chemical non-equilibrium as they both play a role in altering the flow field, especially in terms of recompression shock and the downstream region.

(4) As flight Mach number increased from 10 to 20, the separation length of the STBLI decreased; the thermochemical non-equilibrium effect was significant to the heat flux at Mach number 10, reaching 11.32%. It can be as high as 17.87% at Mach number 20. Moreover, from the results of cases at Mach numbers 10, 15, and 20, the peak heat flux on the wall using the real gas model with turbulence was approximately proportional to the 11/3rd power of the Mach number. Therefore, the thermochemical non-equilibrium effect must be considered in the thermal protection system design for shock wave/turbulent boundary-layer interaction configurations when it exceeds Mach number 10. This study lays the foundation for aerodynamic designs of next-generation hypersonic vehicles and points toward future research of flow-control techniques.

Declaration of competing interest

The authors declare that they have no known competing financial interests or personal relationships that could have appeared to influence the work reported in this paper.

Acknowledgements

The authors would like to express their thanks for the support from the National Key R&D Program of China (Nos. 2019YFA0405300 and 2019YFA0405203), the Natural Science Foundation of Hunan Province of China (grant number 2020JJ4656) and the National Natural Science Foundation of China (grant number 11702322). Also, the authors thank the anonymous reviewers for some very critical and constructive recommendations on this survey.

References

[1] D.V. Gaitonde, Progress in shock wave/boundary layer interactions, Prog. Aero. Sci. 72 (2015) 80–99, https://doi.org/10.1016/j.paerosci.2014.09.002.
[2] J. Muylaert, F. Cipollini, L. Walpot, H. Ottens, Flight experiments for hypersonic vehicle development expert, in: the RTO AVT Lecture Series on "Critical Technologies for Hypersonic Vehicle Development", the von Kármán Institute, Rhode-St-Genèse, Belgium, 10-14 May, 2004. RTO-EN-AVT-116.
[3] L. Fei, M. Choudhari, M. Chang, C.L. Kimmel, D. Adamczak, M. Smith, Transition analysis for the ascent phase of HIFiRE-1 flight experiment, J. Spacecraft Rockets 52 (5) (2015) 1283–1293.
[4] R.L. Kimmel, M.P. Borg, J.S. Jewell, J.H. Miller, D. Prabhu, HIFiRE-5 boundary layer transition and HIFiRE-1 shock boundary layer interaction, Air Force Res. Lab,

Wright–Patterson AFB OH (2015). Aerospace Sys. Directorate. AFRL-RQ-WP-TR-2015-0151.
[5] W. Huang, H. Wu, Y. Yang, L. Yan, S. Li, Recent advances in the shock wave/boundary layer interaction and its control in internal and external flows, Acta Astronaut. 174 (2020) 103–122, https://doi.org/10.1016/j.actaastro.2020.05.001.
[6] J. Gavira, M. Caporicci, F. Ratti, A. Thirkettle, J. Thoemel, EXPERT: the ESA experimental re-Entry test-bed: system overview, in: AIAA/DLR/DGLR International Space Planes & Hypersonic Systems & Technologies Conference, 2011.
[7] J.J. Bertin, R.M. Cummings, Critical hypersonic aerothermodynamic phenomena, Annu. Rev. Fluid Mech. 38 (2006) 129–157, https://doi.org/10.1146/annurev.fluid.38.050304.092041.
[8] J.D. Anderson, Hypersonic and High Temperature Gas Dynamics, second ed., McGraw–Hill, 2006 https://doi.org/10.2514/4.861956.
[9] D. Passiatore, L. Sciacovelli, P. Cinnella, G. Pascazio, Finite-rate chemistry effects in turbulent hypersonic boundary layers: a direct numerical simulation study, Phys. Rev. Fluids. 6 (5) (2021), 054604, https://doi.org/10.1103/PhysRevFluids.6.054604.
[10] L. Kai, L. Jun, L. Weiqiang, Thermal protection performance of magnetohydrodynamic heat shield system based on multipolar magnetic field, Acta Astronaut. 136 (2017) 248–258, https://doi.org/10.1016/j.actaastro.2017.02.011.
[11] G.V. Candler, Rate effects in hypersonic flows, Annu. Rev. Fluid Mech. 51 (2019) 379–402, https://doi.org/10.1146/annurev-fluid-010518-040258.
[12] X.P. Chen, X.L. Li, Direct numerical simulation of chemical non-equilibrium turbulent flow, Chin. Phys. Lett. 30 (6) (2013), 064702, https://doi.org/10.1088/0256-307X/30/6/064702.
[13] L. Duan, M.P. Martín, Assessment of turbulence-chemistry interaction in hypersonic turbulent boundary layers, AIAA J. 49 (2011) 172–184, https://doi.org/10.2514/1.J050605.
[14] L. Duan, M.P. Martín, Assessment of turbulence-chemistry interaction in hypersonic turbulent boundary layers, AIAA J. 49 (2013) 172–184.
[15] C.L. Running, T.J. Juliano, J.S. Jewell, M.P. Borg, R.L. Kimmel, Hypersonic shock-wave/boundary-layer interactions on a cone/flare, Exp. Therm. Fluid Sci. 109 (2019) 109911, https://doi.org/10.1016/j.expthermflusci.2019.109911.
[16] S.L. Gai, A. Khraibut, Hypersonic compression corner flow with large separated regions, J. Fluid Mech. 877 (2019) 471–494, https://doi.org/10.1017/jfm.2019.599.
[17] D. Knight, M. Mortazavi, Hypersonic shock wave transitional boundary layer interactions - a review, Acta Astronaut. 151 (2018) 296–317, https://doi.org/10.1016/j.actaastro.2018.06.019.
[18] K. Zhu, L.-X. Jiang, W.-D. Liu, M.-B. Sun, Q.-C. Wang, Z.-W. Hu, Wall temperature effects on shock wave/turbulent boundary layer interaction via direct numerical simulation, Acta Astronaut. 178 (2021) 499–510, https://doi.org/10.1016/j.actaastro.2020.08.042.
[19] K. Zhu, W.-D. Liu, M.-B. Sun, Impacts of periodic disturbances on shock wave/turbulent boundary layer interaction, Acta Astronaut. 182 (2021) 230–239, https://doi.org/10.1016/j.actaastro.2021.02.017.
[20] D. Knight, O. Chazot, J. Austin, M.A. Badr, G. Candler, B. Celik, D. de Rosa, R. Donelli, J. Komives, A. Lani, D. Levin, I. Nompelis, M. Panesi, G. Pezzella, B. Reimann, O. Tumuklu, K. Yuceil, Assessment of predictive capabilities for aerodynamic heating in hypersonic flow, Prog. Aero. Sci. 90 (2017) 39–53, https://doi.org/10.1016/j.paerosci.2017.02.001.
[21] N.R. Deepak, S.L. Gai, A.J. Neely, A computational investigation of laminar shock/wave boundary layer interactions, Aeronaut. J. 117 (2013) 27–56, https://doi.org/10.1017/S0001924000007740.
[22] M.D. Clemente, M. Marini, S.D. Benedetto, A. Schettino, G. Ranuzzi, Numerical prediction of aerothermodynamic effects on a re-entry vehicle body flap configuration, Acta Astronaut. 65 (2009) 221–239, https://doi.org/10.1016/j.actaastro.2009.01.069.
[23] F.Y. Zuo, S.L. Hu, Thermochemical non-equilibrium effects on aerothermodynamic prediction of laminar double-cone flow, Acta Astronaut. (2021), https://doi.org/10.1016/j.actaastro.2021.01.058.
[24] H.Y. Wang, F. Xie, J. Li, C. Yao, Y.G. Yang, Study on control of hypersonic aerodynamic force by quasi-DC discharge plasma energy deposition, Acta Astronaut. 187 (2021) 325–334, https://doi.org/10.1016/j.actaastro.2021.06.049.
[25] H. Jiang, J. Liu, S. Luo, J. Wang, W. Huang, Hypersonic flow control of shock wave/turbulent boundary layer interactions using magnetohydrodynamic plasma actuators, J. Zhejiang Univ. - Sci. A. 21 (2020) 745–760, https://doi.org/10.1631/jzus.A2000025.
[26] Z. Du, C. Shen, Y. Shen, W. Huang, L. Yan, Design exploration on the shock wave/turbulence boundary layer control induced by the secondary recirculation jet, Acta Astronaut. 181 (2021) 468–481, https://doi.org/10.1016/j.actaastro.2021.01.063.
[27] L. Yan, H. Wu, W. Huang, S. Li, J. Liu, Shock wave/turbulence boundary layer interaction control with the secondary recirculation jet in a supersonic flow, Acta Astronaut. 173 (2020) 131–138, https://doi.org/10.1016/j.actaastro.2020.04.003.
[28] F. Ding, J. Liu, W. Huang, Y. Zhou, S. Guo, Boundary-layer viscous correction method for hypersonic forebody/inlet integration, Acta Astronaut. 189 (2021) 638–657, https://doi.org/10.1016/j.actaastro.2021.09.018.
[29] J. Liu, X. Fan, Y. Tao, W. Liu, Experimental and numerical study on the local unstart mechanism of hypersonic inlet, Acta Astronaut. 160 (2019) 216–221, https://doi.org/10.1016/j.actaastro.2019.04.041.
[30] P.S. Volpiani, Numerical strategy to perform direct numerical simulations of hypersonic shock/boundary-layer interaction in chemical nonequilibrium, Shock Waves 31 (2021) 361–378, https://doi.org/10.1007/s00193-021-01018-6.
[31] F. Grasso, M. Marini, G. Ranuzzi, S. Cuttica, B. Chanetz, Shock-wave/turbulent boundary-layer interactions in nonequilibrium flows, AIAA J. 39 (2001) 2131–2140, https://doi.org/10.2514/2.1209.
[32] X. Wang, C. Yan, W. Zheng, K. Zhong, Y. Geng, Laminar and turbulent heating predictions for mars entry vehicles, Acta Astronaut. 128 (2016) 217–228, https://doi.org/10.1016/j.actaastro.2016.07.030.
[33] Z. Jiang, C. Yan, On the use of thermally perfect gas model for heating prediction of laminar and turbulent SWBLI, Aero. Sci. Technol. 95 (2019) 105484, https://doi.org/10.1016/j.ast.2019.105484.
[34] C. Dai, B. Sun, C. Zhou, C. Zhuo, L. Du, S. Zhou, Numerical investigation of real-gas effect of inward-turning inlet at Mach 12, Aero. Sci. Technol. 115 (2021) 106786, https://doi.org/10.1016/j.ast.2021.106786.
[35] S.B. Pope, Turbulent Flows, first ed., Cambridge University Press, 2000 https://doi.org/10.1017/CBO9780511840531.
[36] N.N. Smirnov, V.F. Nikitin, L.I. Stamov, E.V. Mikhalchenko, V.V. Tyurenkova, Rotating detonation in a ramjet engine three-dimensional modeling, Aero. Sci. Technol. 81 (2018) 213–224, https://doi.org/10.1016/j.ast.2018.08.003.
[37] N.N. Smirnov, V.F. Nikitin, L.I. Stamov, E.V. Mikhalchenko, V.V. Tyurenkova, Three-dimensional modeling of rotating detonation in a ramjet engine, Acta Astronaut. 163 (2019) 168–176, https://doi.org/10.1016/j.actaastro.2019.02.016.
[38] J. Liu, K. Li, W. Liu, High-temperature gas effects on aerodynamic characteristics of waverider, Chin. J. Aeronaut. 28 (2015) 57–65, https://doi.org/10.1016/j.cja.2014.12.004.
[39] Z. Liu, J. Liu, F. Ding, K. Li, Z. Xia, Effect of thermochemical non-equilibrium on the aerodynamics of an osculating-cone waverider under different angles of attack, Acta Astronaut. 139 (2017) 288–295, https://doi.org/10.1016/j.actaastro.2017.07.013.
[40] R.N. Gupta, Reevaluation of flight-derived surface recombination-rate expressions for oxygen and nitrogen, J. Spacecraft Rockets 33 (1996), https://doi.org/10.2514/3.26783, 451–451.
[41] F.R. Menter, Two-equation eddy-viscosity turbulence models for engineering applications, AIAA J. 32 (1994) 1598–1605, https://doi.org/10.2514/3.12149.
[42] F.R. Menter, M. Kuntz, R. Langtry, Ten years of industrial experience with the SST turbulence model, Heat Mass Tran. 4 (2003).
[43] K. Kim, C. Kim, O. Rho, Accurate computations of hypersonic flows using AUSMPW + scheme and shock-aligned grid technique, in: 29th AIAA, Fluid Dynamics Conference, American Institute of Aeronautics and Astronautics, Albuquerque,NM, U.S.A., 1998, https://doi.org/10.2514/6.1998-2442.
[44] K. Li, J. Liu, W. Liu, A new surface catalytic model for silica-based thermal protection material for hypersonic vehicles, Chin. J. Aeronaut. 28 (2015) 1355–1361, https://doi.org/10.1016/j.cja.2015.08.011.
[45] S. Karl, J.M. Schramm, K. Hannemann, High enthalpy cylinder flow in HEG: a basis for CFD validation, in: Aiaa Fluid Dynamics Conference, 2003.
[46] D.V. Gaitonde, An assessment of CFD for prediction of 2-D and 3-D high-speed flows, in: Aiaa Aerospace Sciences Meeting Including the New Horizons Forum & Aerospace Exposition, 2010.
[47] K. Li, J. Liu, W. Liu, Mechanism analysis of Magnetohydrodynamic heat shield system and optimization of externally applied magnetic field, Acta Astronaut. 133 (2017) 14–23, https://doi.org/10.1016/j.actaastro.2016.12.036.
[48] T. Fujino, M. Ishikawa, Numerical Simulation of control of plasma flow with magnetic field for thermal protection in Earth reentry flight, IEEE Trans. Plasma Sci. 34 (2006) 409–420, https://doi.org/10.1109/TPS.2006.872458.
[49] S. Pirozzoli, F. Grasso, T.B. Gatski, Direct numerical simulation and analysis of a spatially evolving supersonic turbulent boundary layer at M=2.25, Phys. Fluids 16 (2004) 530–545, https://doi.org/10.1063/1.1637604.
[50] Y.F. Zhao, Study of Shock Wave/boundary Layer Interaction and Boundary Layer Transition Using High-Order Numerical Scheme, National university of defense technology, Changsha, 2015 (in Chinese).
[51] M. Liu, G. Han, Z. Jiang, Experimental investigation on plate boundary layer transition in JF-12 hypersonic shock tunnel, in: Proceedings of the 32nd International Symposium on Shock Waves (ISSW32 2019), Research Publishing Services, 2019, pp. 399–404, https://doi.org/10.3850/978-981-11-2730-4_0091-cd.
[52] G.T. Coleman, J.L. Stollery, Heat transfer from hypersonic turbulent flow at a wedge compression corner, J. Fluid Mech. 56 (1972) 741, https://doi.org/10.1017/s0022112072002630.
[53] G. Tu, X. Deng, M. Mao, Assessment of two turbulence models and some compressibility corrections for hypersonic compression corners by high-order difference schemes, Chin. J. Aeronaut. 25 (2012) 25–32, https://doi.org/10.1016/S1000-9361(11)60358-0.
[54] X.-H. Zhang, Y.-Z. Wu, J.-F. Wang, Turbulence models for accurate aerothermal prediction in hypersonic flows, Mod. Phys. Lett. B 24 (2010) 1345–1348, https://doi.org/10.1142/S021798491002358X.
[55] N.N. Smirnov, V.B. Betelin, V.F. Nikitin, L.I. Stamov, D.I. Altoukhov, Accumulation of errors in numerical simulations of chemically reacting gas dynamics, Acta Astronaut. 117 (2015) 338–355, https://doi.org/10.1016/j.actaastro.2015.08.013.
[56] N.N. Smirnov, V.B. Betelin, R.M. Shagaliev, V.F. Nikitin, I.M. Belyakov, Yu. N. Deryuguin, S.V. Aksenov, D.A. Korchazhkin, Hydrogen fuel rocket engines simulation using LOGOS code, Int. J. Hydrogen Energy 39 (2014) 10748–10756, https://doi.org/10.1016/j.ijhydene.2014.04.150.
[57] Investigation of unsteady, hypersonic, laminar separated flows over a double cone geometry using a kinetic approach, Phys. Fluids 30 (4) (2018), 046103, https://doi.org/10.1063/1.5022598.
[58] N. Belouaggadia, H. Olivier, R. Brun, Numerical and theoretical study of the shock stand-off distance in non-equilibrium flows, J. Fluid Mech. 607 (2008) 167–197, https://doi.org/10.1017/s0022112008001973.